# Multigap superconductivity and tunneling selectivity of $2H$-$NbSe_2$ : theory and experiment

Y. Noat,[1] T. Cren,[1] V. Cherkez,[1] C. Brun,[1] C. Carbillet,[1] S. Pons,[1] F. Debontridder,[1] D. Roditchev,[1] W. Sacks,[2] L. Cario,[3] J. A. Silva-Guillén,[4] P. Ordejón,[4] A. García,[5] and E. Canadell[5]

[1]*Institut des Nanosciences de Paris, CNRS-UMR 7588, Université Pierre et Marie Curie-Paris 6 UPMC, 4 place Jussieu, 75252, Paris, France*
[2]*IMPMC, Université Paris 6, CNRS, 4 Pl. Jussieu, 75015 Paris, France*
[3]*Institut des Matériaux Jean Rouxel, UMR 6502, 2 rue de la Houssinière, 44322 Nantes, France*
[4]*Centre d'Investigació en Nanociència i Nanotecnologia - CIN2 - (CSIC-ICN), Campus UAB, 08193 Bellaterra, Spain*
[5]*Institut de Ciència de Materials de Barcelona - ICMAB (CSIC), Campus UAB, 08193 Bellaterra, Spain*

(Dated: April 6, 2015)

We have studied $2H$-$NbSe_2$ by scanning tunneling spectroscopy with two different orientations, along the $c$ and the $a/b$ axis. The results can be understood in the framework of a two-gap model: along the $c$-axis, the large gap is dominant in the tunneling spectra, while a smaller gap is measured along the $a/b$ axis. Our measurement thus shows unambiguously the existence of two gaps, where the orientation preferentially selects one gap or the other. Similarly as for $MgB_2$, the tunneling spectra are well described by the McMillan equations for a two-band superconductor, showing that interband coupling originates from quasiparticle scattering from one band to the other. The electronic structure of $2H$-$NbSe_2$ is further studied theoretically by means of DFT calculations. Examining the different contributions to the Fermi level DOS, we conclude that the large gap observed in tunneling originates from states associated with the Fermi surface cylinders around $K$, whereas the small gap originates from the cylinders around $\Gamma$. In addition, we show that the tunneling current at large distance from the surface is dominated by the selenium orbitals. This finding suggests that the third component of the Fermi surface, the Se-based pancake around $\Gamma$, is strongly coupled to the cylinders around $K$, possibly due to the charge density wave state.

PACS numbers:

## I. INTRODUCTION

Superconductivity in niobium diselenide ($2H$-$NbSe_2$) was discovered about fifty years ago [1, 2]. In spite of numerous experimental and theoretical studies of the material, the precise nature of its superconducting (SC) state remains controversial. In particular, the relation between the SC transition [1, 2] and the charge density wave order [3] is still debated.

The possibility of some anisotropy in the SC gap was already noted in the 1970's by Morris et al. [4]. Clear deviations from the standard BCS density of states (DOS) were then observed by Hess et al. [5] using scanning tunneling spectroscopy on a '$c$' axis oriented sample, but were not given much attention at the time. This is surprising since the two-branch Fermi surface (FS), with a set of Nb-derived cylinders around the central $\Gamma$ point of the hexagonal Brillouin zone and another set of cylinders around the corner $K$ points had been well established [6–8]. Later, the gap anisotropy was modeled by Rodrigo et al. [9] using a continuous gap distribution.

More recently, a two-gap scenario was proposed by several groups based on photoemission (ARPES) [10], heat conductivity [11], specific heat [12, 13] or penetration length measurements [14]. In all these works it was assumed that the system is described by the early model of Suhl, Matthias and Walker [15], which assumes a *pair coupling* between the two bands, giving rise to a BCS-like density of states [16]. A particular feature of the Fermi surface of $2H$-$NbSe_2$, a selenium-based pocket near the Brillouin zone center, was first revealed by a combined de Haas-van Alphen and density functional theory (DFT) study, [17] and later confirmed by ARPES Fermi surface mappings [10, 18]. Its role in the multigap scenario has not been determined yet.

The room temperature crystal structure of $2H$-$NbSe_2$ [19, 20] (see Fig. 1) is built from hexagonal $NbSe_2$ layers containing Nb atoms in a trigonal prismatic coordination. The six Nb-Se bonds within these layers are identical (2.598 Å). As shown in Fig.1, the repeat unit of the solid contains two symmetry equivalent layers related by a screw axis along $c$. Successive layers are separated by van der Waals spacings through which there are relatively short Se–Se bonds, i.e. every Se atom makes three Se–Se bonds (3.537 Å) shorter than the sum of the van der Waals radii with the Se atoms of the adjacent layer. The Se–Se bonds along the $c$-direction within the hexagonal layers are even shorter, 3.347 Å. These two structural features give a considerable three-dimensional character to this layered material.

At 30 K $2H$-$NbSe_2$ undergoes a distortion leading to a ($3a\times3a\times c$) superstructure [3]. Its origin has been attributed to a Fermi surface nesting driven charge density wave (CDW) [21] although this explanation has been challenged [7, 8, 18, 22–24]. The detailed structure of the distorted phase has not yet been reported although several models have been discussed [25, 26].

In this paper, the question of multigap supercon-

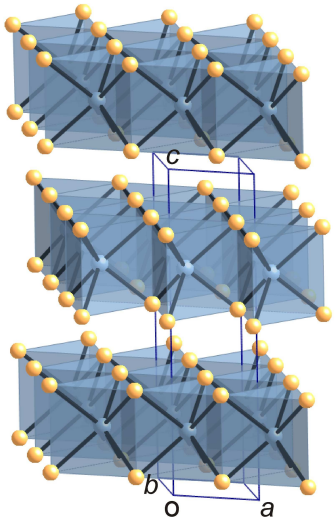


FIG. 1: (Color online) Crystal structure of $2H$-$NbSe_2$. The Nb and Se atoms are represented with blue and yellow spheres, respectively.

ductivity in $2H$-$NbSe_2$ is studied using tunneling measurement in different orientations and its connection to the band structure and Fermi surface is examined. Superconducting-vacuum-superconducting (SIS) configurations were also realized. We show that tunneling measurements in $c$-axis oriented samples of this material can be described in the framework of a two-band model. In addition, a smaller gap is observed along the $a/b$ axis. The SIS data obtained with a nominal $c$-axis oriented sample and a $2H$-$NbSe_2$ tip with $a/b$ orientation confirm this scenario. We further explain why the large gap is dominantly observed along the $c$ axis and show that this tunneling selectivity can be qualitatively understood on the basis of the DFT band structure of the material together with the CDW state coexisting at low temperature.

We finally conclude that $2H$-$NbSe_2$ is a two gap superconductor in many ways similar to $MgB_2$: while superconductivity develops in one band (with a large gap), it is induced in the other band (with a small gap) by means of a proximity effect in reciprocal space (see [27] for $MgB_2$). This effect is adequately described by the McMillan equations [28], where interband coupling arises because of quasiparticle scattering from one band to the other, not taken into account in the Suhl-Matthias-Walker model. The role of the selenium Fermi surface pocket is also discussed.

## II. SCANNING TUNNELING SPECTROSCOPY EXPERIMENT

### A. Tunneling along the $c$ axis

High purity $2H$-$NbSe_2$ was prepared in a sealed tube using the standard iodine vapor transport method. The samples were cleaved under UHV and the tunneling conductance was measured using our home built STM/STS setups at low temperature (Most of the experiments were done at $T = 2.3\ K$; additional measurements in order to explore the fine structure of the gap were done at $T = 300\ mK$ using another setup). Fig. 2 shows a typical tunneling conductance spectrum measured at low temperature with the PtIr tip. As reported previously [5, 9], a well-pronounced gap is observed. However, as shown in the following, this does not mean that only a single gap parameter is present. Indeed, in this case the tunneling conductance shape slightly deviates from a conventional single-gap BCS superconductor.

As shown in a previous report [29], the tunneling conductance can be fitted by the McMillan equations. This model was originally developed in order to describe a thin normal layer coupled to a superconducting layer. It is also relevant to describe a proximity effect in reciprocal space for a multiband superconductor such as $MgB_2$ where a 2D band with high electron-phonon coupling is coupled to a band with 3D character and low electron-phonon coupling [30]. Two gaps are clearly observed in point contact spectroscopy [31] or in tunneling experiments [32–34]. Furthermore, the shape of the excitation spectra follows the McMillan equations and is in agreement with this two band scenario [27, 35].

In this model, a multiband superconductor is described by intrinsic gaps $\Delta_i^0$ resulting from electron-phonon coupling in each band $i$ and it also takes into account the quasiparticle coupling between bands $i$ and $j$, characterized by a coupling parameter $\Gamma_{ij}$, which represents the inverse lifetime of a quasiparticle in band $i$ due to its coupling to band $j$. Such a coupling could result from the presence of impurities [36]. In the clean limit, one cannot exclude the effect of electron-electron scattering. This point remains to be studied by ab-initio calculations including electron correlations.

The interband coupling leads to energy-dependent gaps $\Delta_i(E)$ which can be calculated by the self-consistent equations [28]:

$$\Delta_i(E) = \frac{\Delta_i^0 + \Gamma_{ij}\Delta_j(E)/\sqrt{\Delta_j^2(E) - (E - i\Gamma_{ji})^2}}{1 + \Gamma_{ij}/\sqrt{\Delta_j^2(E) - (E - i\Gamma_{ji})^2}} \quad (1)$$

with $i = 1, 2$. The density of states $N_S(E) = \sum_i N_S^i(E)$ is expressed as a sum over the partial density of states $N_S^i(E)$ in each band $i$:

$$N_S^i(E) = N_i(E_F)\mathrm{Re}\frac{|E|}{\sqrt{E^2 - \Delta_i(E)^2}} \quad (2)$$

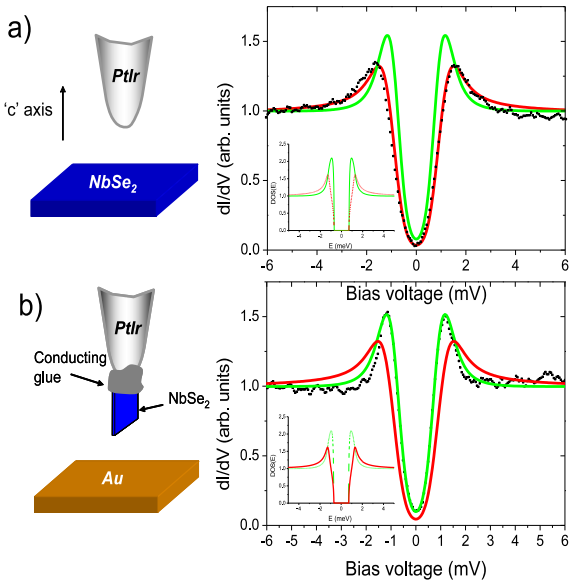


FIG. 2: (Color online) a) Tunneling conductance obtained with a metallic (platinum-iridium) tip in a $c$ axis oriented $2H$-$NbSe_2$ sample. The datas are fitted by a two gap model (McMillan equations) assuming a full tunneling selectivity towards the large gap ($T_L = 1$, in red). It is compared to the situation where the tunneling arises towards the band with a small gap ($T_S = 1$, in green). Inset: Partial DOS corresponding to the small gap and the large gap. b) Tunneling conductance obtained with a $2H$-$NbSe_2$ tip oriented along the a/b axis. The tip is obtained by gluing a $2H$-$NbSe_2$ sample on the slide to a platinum-iridium tip. The data are fitted by a two gap model (McMillan equations) assuming a tunneling selectivity towards the small gap ($T_S = 1$, in green). It is compared (red curve) to the situation where the tunneling arises towards the band with a large gap ($T_L = 1$). The parameters used for the fit in both cases are the following: $T_{fit} = 2.2$K; $\Delta_L^0 = 1.4$ meV; $\Delta_S^0 = 0$ meV; $\Gamma_{SL} = 3$ meV; $\frac{\Gamma_{LS}}{\Gamma_{SL}} = 1/3$. Inset: Partial DOS corresponding to the small gap and the large gap.

To describe the tunneling experiment, we take into account an additional tunneling selectivity. Depending on the configuration in $k$-space and symmetries of the bands relevant to the surface, one particular band or the other can be probed. This effect was clearly demonstrated in magnesium diboride. Indeed, it has been shown that for $c$-axis oriented samples of $MgB_2$, only the small gap is observed in the tunneling density of states [33, 34], while two gaps are clearly seen for an $a/b$ axis oriented sample in grains with arbitrary orientations [32]. This is due to the particular symmetries of the bands in $MgB_2$: the large gap develops in the $\sigma$ band, with high electron phonon coupling and having a rather 2D nature, while a small gap is induced in the $\pi$ band having 3D character [30, 37]. This explains why the small gap is preferentially observed in a nominal $c$-axis oriented sample by scanning tunneling spectroscopy.

Taking into account selectivity effects, the tunneling DOS for a two gap superconductor can be written in the general way:

$$\begin{aligned} N_S(E) &= \sum_{i=1,2} T_i N_i(E_F) \mathrm{Re} \frac{|E|}{\sqrt{E^2 - \Delta_i(E)^2}} \\ &= \sum_{i=1,2} N_i^{eff} \mathrm{Re} \frac{|E|}{\sqrt{E^2 - \Delta_i(E)^2}} \end{aligned} \quad (3)$$

where $T_i$ accounts for the $k$-averaged tunneling probability toward a given band $i$ and $N_i^{eff} = T_i N_i(E_F)$ is the effective DOS in band $i$ as measured by STS taking into account the tunneling selectivity.

It is important to note that the interband quasiparticle coupling leads to characteristic signatures in the excitation spectra which deviates from the standard BCS form [29]. This is at odds with the case of interband pair coupling as considered by Suhl et al. [15] which gives rise to a standard BCS DOS for each band. From the curve fit we deduce the values of the intrinsic gaps in each band $\Delta_0^i$, as well as the interband coupling parameters $\Gamma_{ij}$. Note that the ratio of the partial DOS of two bands is directly related to the interband coupling between them:

$$\frac{\Gamma_{ij}}{\Gamma_{ji}} = \frac{N(E_F^j)}{N(E_F^i)}$$

This information will be very useful and will allow us to compare with the results of bulk measurements such as specific heat.

For $2H$-$NbSe_2$, we get from the fits: $\Delta_L^0 = 1.4 \pm 0.1$ meV and $\Delta_S^0 = 0.00 \pm 0.1$ meV. In order to confirm the fine structure of the gap, additional measurements were also done at $T = 300\ mK$, using another setup (home built STM/STS). The tunneling conductance and the corresponding fit with the two-gap model is plotted in Fig. 3a [38].

In Fig. 3b we show the partial DOS of $2H$-$NbSe_2$ deduced from these fits. Each curve is clearly different from the usual BCS DOS. In particular, a distinctive kink is noticeable at the small gap energy (see arrows in Fig. 3b) in the partial DOS corresponding to the large gap.

With this analysis we find that superconductivity preferentially develops in one band while Cooper pairs arise in the other by the proximity effect, as previously mentioned. This is analogous to the case of $MgB_2$ where superconductivity develops in the $\sigma$ band and is induced in the $\pi$ band [30]. The values for the interband coupling parameters are: $\Gamma_{SL} = 3 \pm 0.3$ and $\frac{\Gamma_{LS}}{\Gamma_{SL}} = 1/3 \pm 0.03$. The ratio of the coupling parameters is given by the ratio of the partial DOS at the Fermi energy of the corresponding bands: $\frac{\Gamma_{12}}{\Gamma_{21}} = \frac{N_2(E_F)}{N_1(E_F)}$. Thus, knowing the contributions of the different bands in the DOS would

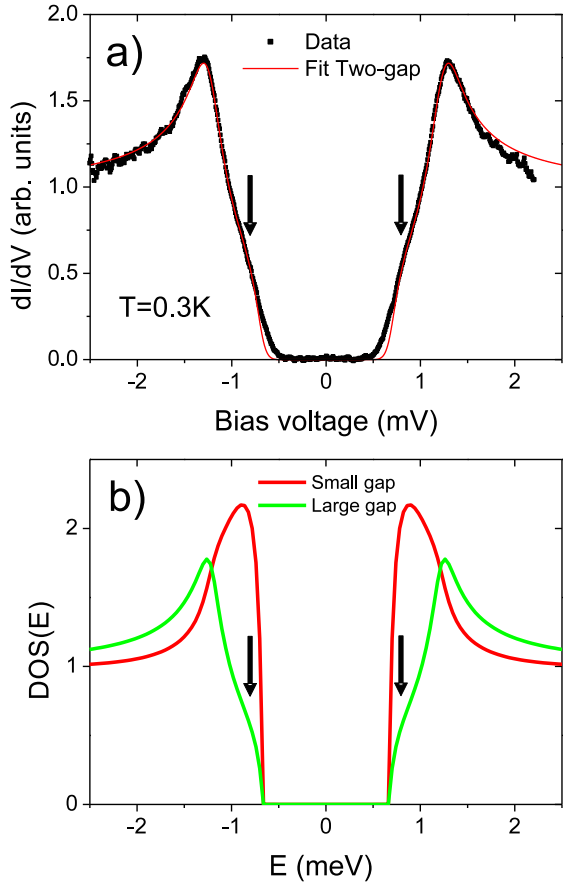


FIG. 3: (Color online) a) Tunneling conductance obtained with a metallic (platinum-iridium) tip in a $c$ axis oriented $2H$-$NbSe_2$ sample at T=300mK. The datas are fitted by a two-gap model (McMillan equations) assuming a full tunneling selectivity towards the large gap ($T_L = 1$, in red). The parameters used for the fit are the following: $T_{fit} = 2.2$K; $\Delta_L^0 = 1.32$ meV; $\Delta_S^0 = 0$ meV; $\Gamma_{SL} = 2.5$ meV; $\frac{\Gamma_{LS}}{\Gamma_{SL}} = 1/4$. b) Partial DOS for the small (in red) and large gap (in green) for the parameters deduced from the fits (shown in Fig. 2). $\Delta_L^0 = 1.3$ meV; $\Delta_S^0 = 0$ meV; $\Gamma_{SL} = 2.5$ meV; $\frac{\Gamma_{LS}}{\Gamma_{SL}} = 1/4$.

help identify in which band superconductivity develops preferentially (i.e. the band with a large SC gap). Note that the respective weights in the DOS for the small and large gaps are in *qualitative agreement* with the values deduced from the temperature and magnetic field dependence of the specific heat measurements [12]. Fitting their data with a simple two-band model (i.e. the model of Suhl et al. [15]), Huang et al. [12] found a ratio close to 1/4 with gap values $\Delta_S = 0.73$ meV and $\Delta_L = 1.26$ meV while Ying et al [13] found a ratio 0.56 with gap values $\Delta_S = 0.85$ meV and $\Delta_L = 1.5$meV.

The tunneling selectivity in $2H$-$NbSe_2$ appears to be also very sensitive to cleavage conditions. When the cleavage was done under UHV conditions, the large gap dominates in the tunneling current, i.e. $T_L \approx 1$. On the other hand when the sample is cleaved in air, the tunneling selectivity varies and a combination of the small and large gaps is necessary to fit the data properly ($0 \leq T_S \leq 0.5$). We propose that this effect is related to modifications in the Se pocket arising with surface contamination when the sample is cleaved in air.

### B. Tunneling along the $a/b$ axis

In a second step, we have measured the tunneling conductance for a $2H$-$NbSe_2$ sample with a different orientation. For this purpose, we have fabricated special tips with $2H$-$NbSe_2$ samples glued on their side on a standard platinum-iridium tip (see schematics in Fig. 2b). A typical conductance spectrum is shown in Fig. 2, with a fit using the two-gap proximity effect model as described previously, with the tunneling selectivity towards the small gap and, for comparison, towards the large gap. The other parameters are unchanged in the fits within the uncertainty mentioned above. For this orientation, it is clear from the fit that the small gap is dominantly probed, as opposed to the nominal $c$-axis experiment. This demonstrates that the tunneling selectivity depends clearly upon the sample orientation.

This important point is further checked by using a Superconductor-Insulator-Superconductor (SIS) junction with a $2H$-$NbSe_2$ tip and a $c$-axis oriented sample. For a SIS junction, the tunneling current is given by

$$I(V,z) = I_0 \exp(-2\,\alpha_k\, z)\times \int_E N_{tip}(E) \quad N_{sample}(E+eV)\times [f(E) - f(E+eV)]\, dE$$

where $f(E)$ is the Fermi-Dirac function, $N_{tip}(E)$ and $N_{Sample}(E)$ are respectively the DOS of the tip and the sample. As shown in Fig. 4, the SIS tunneling conductance is well fitted assuming that a full tunneling selectivity towards the small gap for the tip (i.e. $T_S$ =1 and $T_L$ =0) and towards the large gap for the sample (i.e. $T_S$ =0 and $T_L$ =1), therefore confirming the previous results.

### C. Temperature dependence of the tunneling conductance

The tunneling spectra for a SIS junction (see Fig. 5b, $2H$-$NbSe_2$ tip-$2H$-$NbSe_2$ sample) as well as for SIN junction (see Fig. 5a, $2H$-$NbSe_2$ tip-gold sample) was measured as a function of temperature. The conductance curves were fitted at each temperature with the McMillan model for a two-gap superconductor described in section II. The same parameters were used for both SIS and SIN junctions.

From the fits, we deduce the temperature dependence of the intrinsic gaps $\Delta_L^0(T)$ and $\Delta_S^0(T)$. Note that $\Delta_S^0(T)$

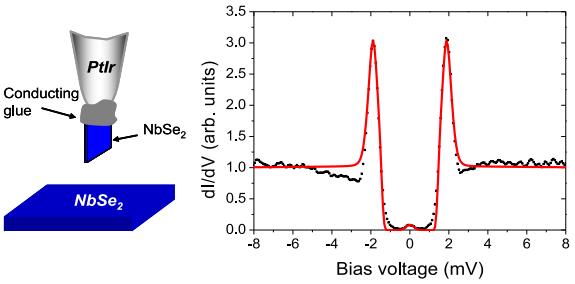


FIG. 4: (Color online) Left: Scheme of the tunneling junction: The tip is oriented in the $a/b$ axis while the sample is '$c$' axis oriented. Right: Tunneling conductance of the SIS junction. The spectrum is fitted with the McMillan model, assuming a tunneling selectivity towards the small gap for the tip ($T_S = 1$; $T_L = 0$) and the large gap for the sample ($T_S = 0$; $T_L = 1$) . The tip and sample are described by the same parameters as before.

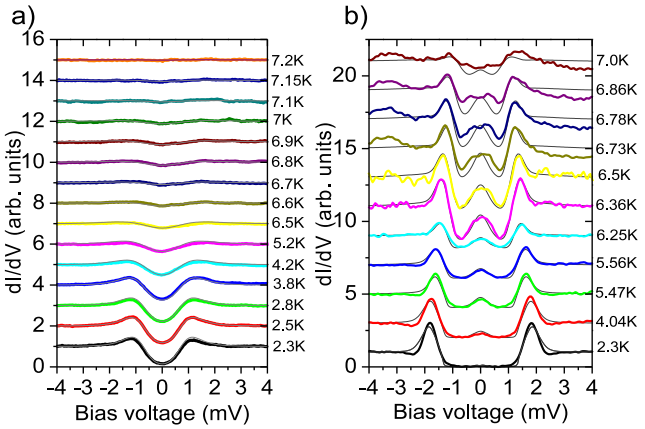


FIG. 5: (Color online) a) Temperature dependence of the tunneling conductance obtained for a SIN junction with a $2H$-$NbSe_2$ tip and a gold sample and corresponding McMillan fit (in gray). b) Temperature dependence of the tunneling conductance obtained for a SIS junction with a $2H$-$NbSe_2$ tip and a '$c$' axis oriented sample, and corresponding McMillan fit (in gray). The data are fitted with the McMillan model for a two gap superconductor with the same parameters for the tip and sample: $\Delta_S^0$ =0 meV; $\Gamma_{SL}$ =3 meV; $\Gamma_{LS} = \frac{N_S(E_F)}{N_L(E_F)} = \Gamma_{SL}/3$. The intrinsic large gap $\Delta_L^0$ is the adjustable parameter. The tip is oriented in the $a/b$ axis while the sample is $c$ axis oriented. In the SIS case, the spectra are fitted with the McMillan model, assuming a tunneling selectivity towards the small gap for the tip ($T_S = 1$; $T_L = 0$) and towards the large gap for the sample ($T_S = 0$; $T_L = 1$). In the SIN case, we assume a full tunneling towards the small gap ($T_S = 1$; $T_L = 0$). At each temperature, the fit gives the value of the intrinsic large gap $\Delta_L^0(T)$.

is close to zero for all temperatures. In addition, the theoretical dependence of the intrinsic gaps with temperature

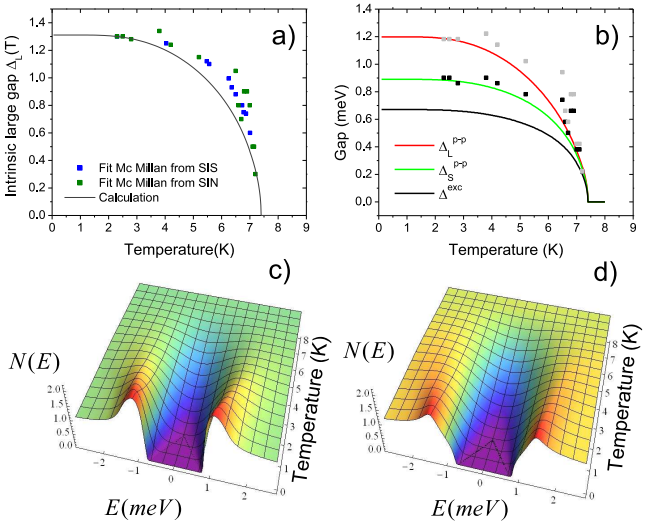


FIG. 6: (Color online) a) Temperature dependence of the intrinsic large gap $\Delta_L^0(T)$ deduced from the fits for the SIN ($2H$-$NbSe_2$ tip-gold sample) and SIS junction ($2H$-$NbSe_2$ tip-$2H$-$NbSe_2$ sample) compared to the theoretical value $\Delta_L^{0,th}(T)$ calculated by the resolution of the self-consistent equations (4). b) Theoretical temperature dependence of the excitation gap $\Delta^{ex,th}$ (in black) and of the peak to peak small and large gaps (in red and green respectively) $\Delta_{S,L}^{pp,th}$ which are defined as the peak to peak value in the calculated partial DOS for the small and large gap $N_S(E)$ and $N_L(E)$. c) Temperature dependence of the partial DOS for the small gap $N_S(E)$ calculated by the resolution of the self-consistent equation. d) Temperature dependence of the partial DOS for the large gap $N_L(E)$.

can be obtained from the self-consistent equations:

$$\Delta_i^0 = \lambda_{ii} \int_0^{\hbar\omega_i} \mathrm{d}E \tanh\left[\frac{E}{2k_BT}\right] \mathrm{Re}\left[\frac{\Delta_i(E)}{\sqrt{E^2-\Delta_i^2(E)}}\right] + \lambda_{ij}\sqrt{\frac{N_j}{N_i}} \int_0^{\hbar\omega_{ij}} \mathrm{d}E \tanh\left[\frac{E}{2k_BT}\right] \mathrm{Re}\left[\frac{\Delta_i(E)}{\sqrt{E^2-\Delta_i^2(E)}}\right] \quad (4)$$

where $\lambda_{ii} = V_{ii}N_i$ are the intraband electron-phonon coupling constants in each band, while $\lambda_{ij} = V_{ij}\sqrt{N_iN_j}$ is the interband electron-phonon coupling constant of the Suhl-Matthias-Walker model [15].

In the most general case, the intrinsic gaps result from intraband and interband pair coupling [15]. In the special case of $2H$-$NbSe_2$, interband pair coupling can be neglected (but not interband quasiparticle scattering), i.e. $\lambda_{12} = 0$ and only the large intrinsic gap is not zero, $\lambda_{11} = 0$ for the small gap and $\lambda_{22} \approx 0.5$ for the large gap, with the corresponding phonon frequency $\hbar\omega_2 \approx 6.55$ meV. This shows unambigously that the small gap is induced by proximity effect as a result of quasiparticle interband coupling, similarly as for $MgB_2$ [27].

The temperature dependence of the intrinsic large gap deduced from the fits $\Delta_L^0(T)$ can then be compared to the theoretical expectation $\Delta_L^{0,th}(T)$(see in Fig. 6 the temperature dependence of the DOS for the small and large gap bands form which we deduce $\Delta_L^{0,th}(T)$). From the

calculation, we also deduce the theoretical dependence of the peak to peak gap $\Delta_{S,L}^{pp,th}$ in the small/large partial DOS $N_{S,L}(E)$ as well as of the excitation gap $\Delta^{ex,th}$ (Fig 6b), which can also be compared to the values deduced from the fit, showing a qualitative agreement.

### D. Two band model vs distribution of gaps

As already mentioned, the tunneling conductance in $2H$-$NbSe_2$ was interpreted in terms of a continuous gap distribution [9]. In this model, the tunneling DOS is described by a weighted sum of BCS DOS: $N(E) = \sum_i g(\Delta_i) N_{BCS}(E, \Delta_i)$. We have determined the gap distribution needed to fit the DOS of the large and small gap, which were calculated by solving the self-consistent equations in the McMillan model (see Fig. 6c,d). The distributions are shown in Fig. 7.

The distribution for the large gap exhibits two well defined peaks around 0.77meV and 1.16meV. One notes that their positions correspond to the peak-to-peak gaps in the McMillan DOS (see Fig. 6a,b). The distribution of the small gap is strikingly different from that of the large gap. In particular, it exhibits a single peak at 0.76meV. More importantly, one notices that some of the weights have negative values, which demonstrate that it is not possible to properly fit the small gap with a gap distribution with only positive weights. This is due to the very peculiar shape of the peaks, whose amplitude decreases more rapidly than $\sim 1/\sqrt{E-\Delta}$ close to the gap edge. The same result would of course have been obtained by directly fitting the conductance curve obtained in the tunneling experiment with the tip oriented in the a/b axis. Thus, while the conductance for the large gap can be fitted by a gap distribution, this is not the case for the small gap.

In addition, for both the small and large gap, the distribution is more and more peaked as the temperature increases and gets very close to BCS, with a same gap value for both bands near the critical temperature. This behavior is quite opposite to that expected from the Suhl, Matthias and Walker model [15], where the ratio between the two gaps increases with the temperature. Thus, the criteria of homogeneization of the two gaps towards a single BCS like signature close to $T_C$ is a marked characteristic of a quasiparticle mediated interband coupling (as in Schopohl and Scharnberg's model [36]) instead of a Cooper pair interband coupling (as in the Suhl, Matthias and Walker model) [15].

To conclude, this series of experiments leads to three major conclusions:

i) Our data for $2H$-$NbSe_2$ can be explained in terms of a two-band proximity effect.

ii) The tunneling selectivity is important to fit the superconductor-insulator-normal-metal (SIN) spectra.

iii) Tunneling towards $c$-axis gives a large gap while tunneling towards $a/b$ axis gives a small gap.

However, two points remain to be elucidated:

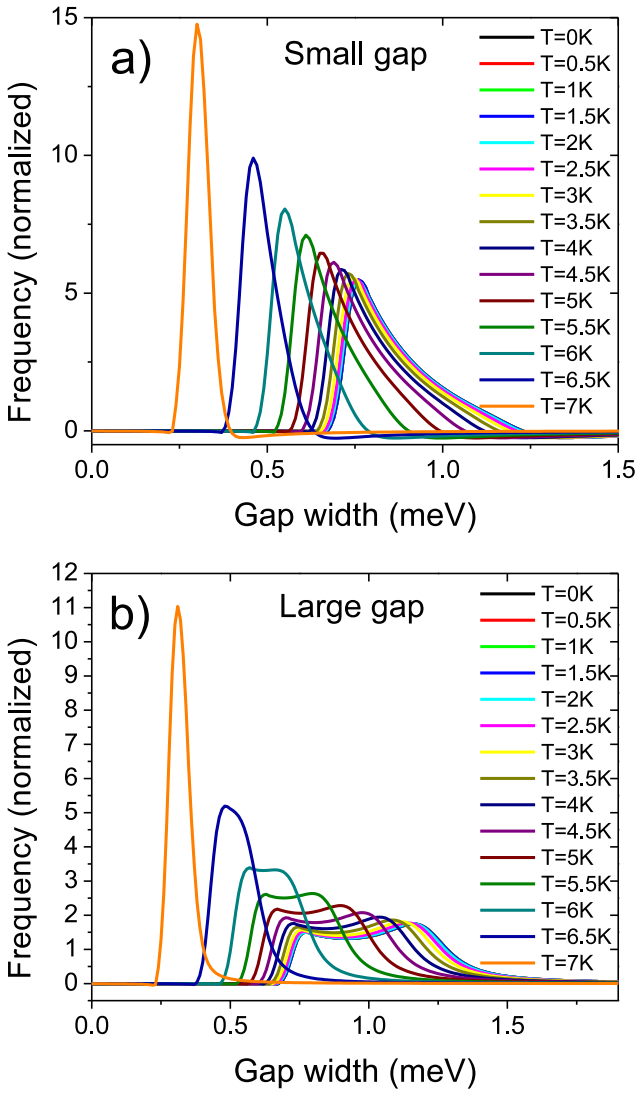


FIG. 7: (Color online) Small (a) and large (b) gaps distributions obtained by fitting the DOS calculated self-consistently as a function of temperature with a weighted sum of BCS DOS, following the fitting procedure of Rodrigo et al. [9].

i) Which band corresponds to which gap?

ii) As it is now well established [17], the Se bands offer an additional branch of the Fermi surface, so its role must be elucidated.

To clarify these aspects, we first discuss the electronic structure and tunneling of $2H$-$NbSe_2$ on the basis of first-principles DFT calculations, and later we consider the possible role of the low temperature CDW transition occurring in this material.

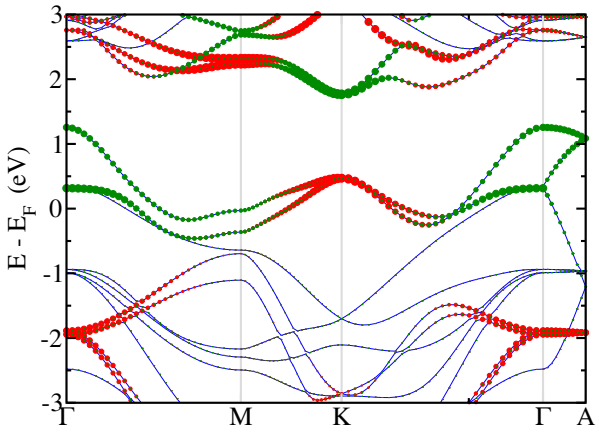


FIG. 8: (Color online) Calculated band structure for $2H$-$NbSe_2$ where the green and the red circles are proportional to the niobium $d_{z^2}$ and $d_{xy}/d_{x^2-y^2}$ character, respectively. Γ = (0, 0, 0), $M$ = (1/2, 0, 0), $K$ = (1/3, 1/3, 0), $A$ = (0, 0, 1/2), $L$ = (1/2, 0, 1/2) and $H$ = (1/3, 1/3, 1/2) in units of the reciprocal hexagonal lattice vectors.

## III. DFT CALCULATIONS

### A. Electronic structure of $2H$-$NbSe_2$

The electronic structure of $2H$-$NbSe_2$ has been calculated a number of times in the literature [17, 18, 22, 23, 39–41]; here we just highlight some aspects which are relevant in order to understand the signatures of multigap superconductivity in tunneling spectroscopy. The calculated band structure is shown in Fig. 8. The details of the calculations are given in Appendix A. There are three partially filled bands, the two upper ones having niobium 4$d$ as the dominant character (except around Γ) whereas the lower is mostly based on selenium orbitals. From now on these bands will be referred to as band 3, 2, and 1, respectively. This is in contrast with the situation for a single $NbSe_2$ slab where only the two niobium 3$d$ based bands are partially filled.

The calculated Fermi surface (see Fig. 9) contains three different contributions. First, a pancake like contribution centered at the Γ point arising from the selenium based band. Second a pair of warped cylinders centered at Γ arising from the two partially filled niobium 3$d$ bands. Third, a pair of warped cylinders centered at $K$ arising also from the two partially filled niobium 3$d$ bands. The cylinders occur in pairs because there are two layers per repeat unit and thus there are in-phase and out-of-phase combinations of the former niobium bands. The two cylinders around Γ as well as those around $K$ merge at the border of the Brillouin zone because there the phase factors are such that the interlayer interactions vanish. Although both pairs of cylinders around Γ and $K$ originate from the same bands their character completely changes from one region to the other: Whereas the niobium character is mostly $d_{z^2}$ around Γ it is $d_{xy}/d_{x^2-y^2}$ around $K$ (see Fig. 8).

### B. Contribution of the different orbitals to the partially filled bands

In correlating the partially filled bands to the STM images it will be essential to have a clear idea of what is the relative weight of the different orbital contributions, i.e. niobium $d_{z^2}$, niobium $d_{xy}/d_{x^2-y^2}$ and selenium, for the different parts of the Fermi surface (i.e. in the two different pairs of cylinders and in the pancake around Γ). The pancake is strongly based on the selenium orbitals. Of particular interest are the middle and upper partially filled bands. Their orbital contributions are shown in Fig. 10. An important observation is that the selenium contribution to these formally niobium bands is comparable to the individual niobium contributions. As shown in Fig. 11, almost half of this selenium contribution is $p_z$, i.e., the selenium orbitals perpendicular to the layers. This means that although globally the metal character prevails in these two bands, there is a very important hybridization of the selenium orbitals, and particularly the selenium $p_z$ orbitals. Consequently, they are expected to dominate the tunneling along the $c$ axis (see the calculation of the tunneling current in section III D), and Se atoms will be seen in the tunneling images, at least at large distance.

### C. Partial DOS associated with the different portions of the Fermi surface

Shown in Table I is the partitioning of the total niobium and selenium contributions to the density of states at the Fermi level into those associated with the cylinders around Γ and those around $K$ for the middle and upper partially filled bands as well as for the pancake around Γ. The more salient features of the second and third columns of this table are:

i) The contributions of the upper niobium-based band are considerably larger.

ii) For both niobium-based bands the contribution of the cylinders around K are always larger than those of the cylinders around Γ.

iii) The contribution of the lower selenium band is small.

iv) The ratio between the contribution of the $K$ vs. Γ cylinders to the total DOS at the Fermi level is 2.7.

The origin of these values is developed in detail in Appendix A. As noted above, the selenium contribution to the niobium-based bands is very important and a substantial portion is due to the $p_z$ orbitals pointing outside the layers so that these contributions will most certainly dominate in the tunneling current. From the values of the second and third column of this table, which of course refer to values for bulk $2H$-$NbSe_2$, one could expect a large

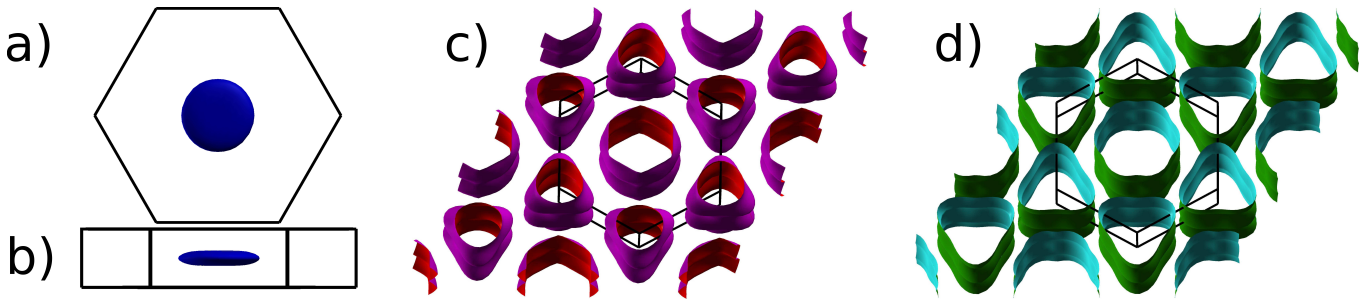


FIG. 9: (Color online) Contribution of band 1 (a and b), band 2 (c) and band 3 (d) to the Fermi surface for $2H$-$NbSe_2$.

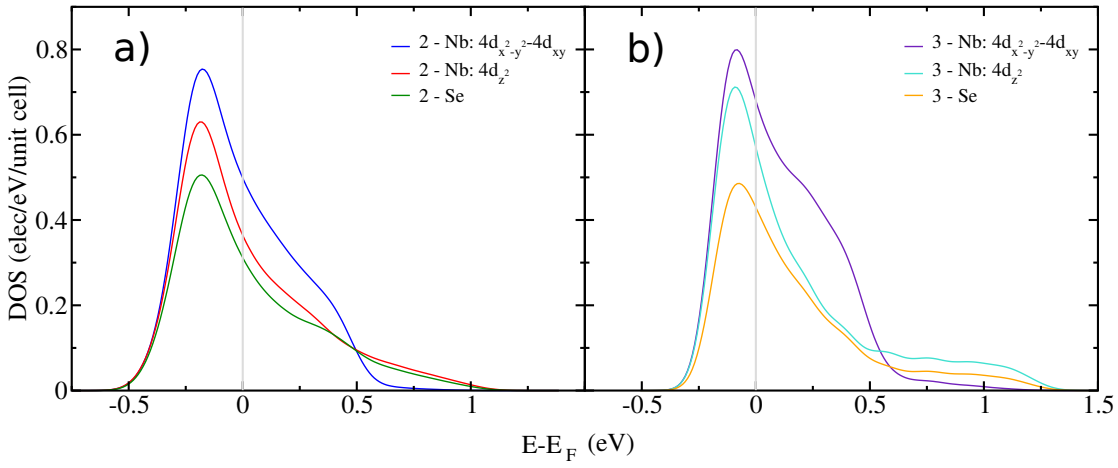


FIG. 10: (Color online) Separate contributions of the selenium, niobium $d_{z^2}$ and niobium $d_{xy}/d_{x^2-y^2}$ orbitals to the density of states associated with the (a) middle -2- and (b) upper -3- partially filled bands.

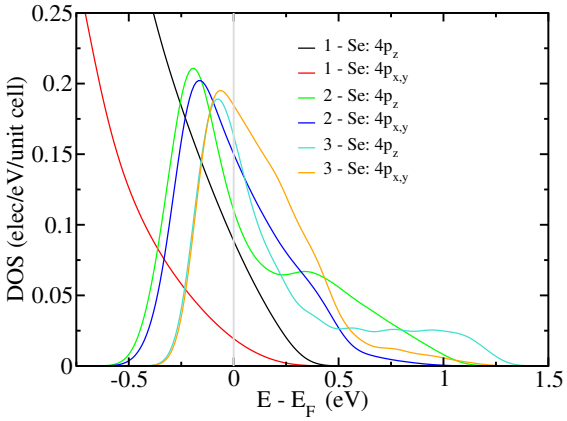


FIG. 11: (Color online) Separate contributions of the selenium $p_z$ and selenium $p_{x,y}$ orbitals to the lower (1), middle (2) and upper (3) partially filled bands.

contribution from the cylinders around $K$, a lesser contribution from the cylinders around $\Gamma$, and finally an even smaller contribution from the selenium based pancake. Surprisingly, this is not what is found in the calculation, as shown in the following.

### D. Calculated tunneling images

We now consider STM imaging within the Tersoff-Hamman approximation, [42] where the current at a given tip position is proportional to the LDOS at that point, integrated over the standard energy window given by the tip-surface potential difference $(E_F, E_F + eV)$.

In this model, the calculated images correspond to constant current images, showing the maps of heights that produce a constant tip-surface current. Instead of specifying the value of the current (which is the situation in an experiment), we choose a particular value of the density of states and plot the corresponding constant DOS surface. In Fig. 12 we show the STM images for a specific isovalue, separating the different contributions of the pancake, the cylinders around $\Gamma$ and the cylinders around $K$. As pointed out in section III A, when dealing with tunneling spectroscopy along the $c$ axis, the contribution to the tunneling due to the three portions of the Fermi surface should be dominated by those of the selenium atoms. Thus, it is expected that the three images will be practically identical, i.e. they will be made of bright spots centered at the selenium atom positions, though with different intensities. As shown in Figs. 12a to 12c this is indeed the case, in agreement with experimental

TABLE I: Total and partial DOS for the different bands at the Fermi level around Γ and $K$, given in elec·(eV· unit cell)$^{-1}$.

| | DOS (Total) | DOS (Nb contribution) | DOS (Se contribution) | DOS ($Se_{p_z}$ contribution) |
|---|---|---|---|---|
| Band 1 Γ | 0.117 | 0.035 | 0.080 | 0.062 |
| Band 2 Γ | 0.359 | 0.239 | 0.121 | 0.066 |
| Band 2 $K$ | 0.731 | 0.528 | 0.203 | 0.052 |
| Band 3 Γ | 0.337 | 0.260 | 0.080 | 0.032 |
| Band 3 $K$ | 1.175 | 0.848 | 0.331 | 0.117 |

results (note however that for small tip-surface distances, the underlying Nb atoms have been also experimentally seen in the tunneling images [43]). This calculation also shows that the Se contribution for the three different Fermi surface portions plays a crucial role in the tunneling, as discussed in the previous section.

### E. Tunneling selectivity

The key aspect when trying to use the calculated images in understanding the origin of the proposed two-gap superconductivity in this material lies in evaluating the relative weight in the tunneling current due to each of the three components of the Fermi surface. The results can be compared with the STM measurements. From the Tersoff and Hamman analysis [42], it is expected that the contribution of the states with small wave vector parallel to the surface will decay slower in vacuum and thus give a dominant contribution to the current for large tip-surface distance. Tersoff and Hamman also stressed the importance of states near the Brillouin zone boundary which also give a significant contribution.

A precise analysis requires the calculation of the tunneling current as a function of the height of the tip, which reflects how the different contributions in the DOS decrease in vacuum. We have studied the decay of the current $I(z)$ with the tip height $z$ in different positions of the $x, y$ plane for the three different components of the image. For this purpose, we calculate $I(z)$ at different $(x, y)$-plane positions, which is expected to roughly vary exponentially $I \approx Ae^{-\alpha z}$. If the exponential dependence holds, we can easily obtain $\alpha$ by doing a fit of the data.

In some cases, the curves do not correspond to a single exponential, but rather display two exponential regimes (with two different slopes). This can also be understood within the Tersoff and Hamman model [42]. Far from the surface (where the potential is roughly constant and equal to the vacuum potential), the wave functions can be expressed as:

$$\psi_{\mathbf{k}}(x, y, z) = \sum_{G_x} \sum_{G_y} C_{\mathbf{k}}(\mathbf{G}) e^{i(\mathbf{G}+\mathbf{k})\cdot\mathbf{r}} e^{-\alpha_{\mathbf{k}+\mathbf{G}} z}, \qquad (5)$$

where $C_{\mathbf{k}}(\mathbf{G})$ is the Fourier component of the wavefunction at a reference plane (taken as z = 0), $\mathbf{G} = (G_x, G_y)$ the surface reciprocal lattice vectors and $\mathbf{r} = (x, y)$ is the in-plane position. The decay of the corresponding Fourier component with $z$ is thus given by

$$\alpha_{\mathbf{k}+\mathbf{G}} = \sqrt{\kappa^2 + (\mathbf{k}+\mathbf{G})^2}, \qquad (6)$$

where $\kappa^{-1}$ is the standard decay length depending on the work function.

From this formula, it is apparent that the wave functions have different components with different decay into the vacuum. The decay length of a given state depends on the $\mathbf{G}$ vector of that component, and on the parallel surface momentum $\mathbf{k}$. At large distances from the surface, the $\mathbf{G} = \mathbf{0}$ component will dominate, with a decay $\alpha_{\mathbf{k}} = \sqrt{\kappa^2 + \mathbf{k}^2}$. In this case, the decay of the wave function is determined by both the work function and the wave vector of the states at the Fermi surface near the Γ point. For distances closer to the surface, several $\mathbf{G}$ will contribute, leading to different decay rates. The results of the fits to $I(z)$ are shown in Table II. A second exponential is needed in the component of the cylinders around $K$, indicating a faster decay of one contribution of the partial DOS relatively close to the surface.

### F. Contribution of Nb-cylinders to the tunneling current

The ratio of the DOS in vacuum associated with the cylinders around Γ and the cylinders around $K$ plotted as a function of the distance from the surface is shown in Fig. 13. For most values of the tip to surface distance, the intensity due to the cylinders around Γ is around twice larger than that originating from the cylinders around $K$. This surprising result might be explained thought consideration of both tunneling selectivity and the signs of the mixing coefficients of the orbitals for a given wave vector (see the discussion in appendix A).

To make some progress in understanding the origin of the different gaps we should now consider the Se based pancake portion of the Fermi surface. Three-quarters of its contribution to the density of states at the Fermi level originate from the Se $p_z$ orbitals so that some degree of interband coupling with the cylinders around Γ and $K$ might be expected. As a matter of fact, if one associates the contributions of the Nb-cylinder around $K$ and the Se pocket, it then becomes the dominant contribution when

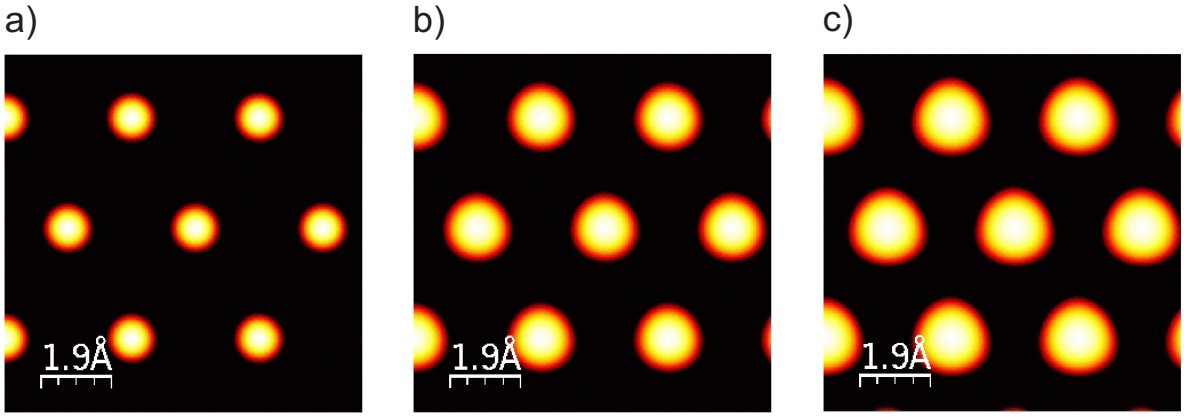


FIG. 12: (Color online) STM images associated with the pancake contribution (a), the cylinders around Γ (b), and the cylinders around $K$ (c). Note that the scale for the three images is different.

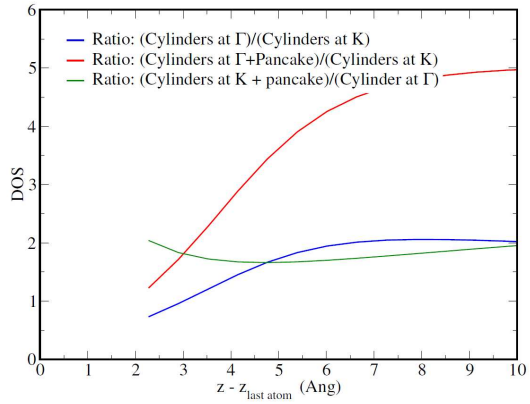


FIG. 13: (Color online) Ratio of the STM image intensities at different distances from the surface.

compared to that of the Nb-cylinder around Γ (Fig. 13, green curve). Remind that this occurs despite the dominance of the bare contribution of the cylinders around Γ over that of the cylinders around $K$. This observation reinforces our suspicion that the Se pancake pocket may play a crucial role in the tunneling current through interband coupling with either the cylinders around Γ or $K$. Thus this question is further addressed in the following section.

## IV. ONE OR TWO GAPS? COMPARISON OF EXPERIMENTAL RESULTS

### A. Anisotropy vs two-gap superconductivity

As described in section I, $2H$-$NbSe_2$ cannot be simply described by the BCS theory for a isotropic 's' wave superconductor: Clear deviations from conventional BCS behavior were observed in the tunneling spectra [5] or in the field dependence of the $\gamma$ coefficient in the specific heat [11, 13, 44, 45]. The origin of these deviations was addressed by means of many experimental techniques: specific heat [12, 13], heat transport [11], penetration length [14] and scanning tunneling spectroscopy [9, 29]. The results are summarized in Table III. They can be sorted into two groups, either concluding that $2H$-$NbSe_2$ is a two-gap superconductor [11, 12, 29] or that the gap is anisotropic in $k$-space [46]. Some works [13, 14] suggest that the experimental results could be interpreted in both ways.

It is important to note that in order to fit specific heat or penetration depth data [12–14], it was implicitly assumed that the DOS is a weighted sum of BCS DOS with two different gap values. This is equivalent to the pioneering model of Sulh, Matthias, Walker [15] for a two-gap superconductor, where the two corresponding bands are coupled with an interband pair coupling term. In fact, a different coupling between the bands must be considered to precisely reproduce the shape of the tunneling spectra (see section II).

### B. Photoemission results

ARPES results recorded for $2H$-$NbSe_2$ are often contradictory [47–52]. The limited resolution of the photoemission, of the order of twice the superconducting gap, and the low critical temperature of this material makes the data difficult to analyze. Moreover, the transition to the CDW state, whose origin and consequences on the spectral weight and superconducting state are still debated, complicates the determination of the spectral modification at the Fermi energy $E_F$ near the SC critical temperature. Yet, some general features emerge from the analysis of the more recent fine ARPES experiments (see table IV for a comparison of reported photoemission results): a large gap is shown to open in the Nb cylinders around $K$ while a smaller gap is found associated with the Nb Γ-cylinders. There is no indication of the exis-

TABLE II: $I$ vs $z$ fits

| **Contribution** | **Position** | $\alpha$**-exp 1 (Bhor$^{-1}$)** | $\alpha$**-exp 2 (Bhor$^{-1}$)** |
|---|---|---|---|
| Pancake | At atom | 1.3049 ± 0.0011 | - |
| | At hollow | 1.3016 ± 0.0004 | - |
| Cylinder at Γ | At atom | 1.3144 ± 0.0016 | - |
| | At hollow | 1.3093 ± 0.0007 | - |
| Cylinder at $K$ | At atom | 1.3066 ± 0.0006 | 1.66 ± 0.04 |
| | At hollow | 1.3064 ± 0.0006 | - |

TABLE III: Comparative of experimental results for $2H$-$NbSe_2$ concerning the anisotropy vs two-gap superconductivity.

| Work | Experiment | Model | Gap value(s) (meV) |
|---|---|---|---|
| Huang et al [12] | Specific heat | Two isotropic gaps (fit) | $\Delta_S$ =0.73, $\Delta_L$ =1.26<br>Weights: 20%; 80% |
| Ying et al. [13] | Specific heat | Two isotropic gaps (fit) | $\Delta_S$ =0.85, $\Delta_L$ =1.5<br>Weights: 36%; 64% |
| ” | ” | Anisotropic gap (fit)<br>$\Delta = \Delta_0 \left[0.4 + 0.6\vert\cos(3\theta)\vert\right]$ | $\Delta_0$=1.62 |
| Rodrigo et al. [9] | Scanning tunneling Spectroscopy | Gap distribution (fit)<br>$N(E) = \frac{1}{\alpha_i}\sum \alpha_i N_{BCS}(\Delta_i, E)$ | Gap values in the range<br>$[0.4 - 1.4]$ |
| Fletcher et al. [14] | Penetration length | Two isotropic gaps (fit) | $\Delta_S$ =0.62-0.67, $\Delta_L$ =0.98-1.27<br>Weights: 0.43-0.5%; 0.57-0.57% |
| ” | ” | Six fold gap<br>$\Delta(\phi, T) = \Delta_{min}(T)\frac{[1+\epsilon\cos(6\phi)]}{1-\epsilon}$ | $\Delta_{min}$ =0.56-0.58<br>$\frac{1+\epsilon}{1-\epsilon}$=1.74-2.33 |
| Boaknin et al. [11] | Heat Conductivity | Two gaps<br>(Deduced from two length scales) | $\frac{\Delta_L}{\Delta_S}$ ∼3 |
| Sanchez et al. [46] | Specific heat | Anisotropic gap (fit)<br>$\Delta_k(T) = \Delta_0(T)(1 - \epsilon_2\cos^2\theta)$ | $\Delta_0(0)$ =1.55;<br>$\epsilon_2$=0.6 |

tence of a gap in the small Se pocket around Γ. However, these results should be taken with care since the ARPES data for the Se $p_z$ pocket are affected by the very strong $k_z$ dispersion (see the band diagram calculations) and/or defects. The selenium $p_z$ states appear strongly blurred in photoemission images and a quantitative analysis of this band is questionable. Indeed, the finding of non-gapped states at the Fermi energy in the Se pocket seem to contradict the existence of a superconducting state. In contrast, STS experiments as well as specific heat measurements clearly imply a fully gapped DOS at $E_F$.

TABLE IV: Comparative of gap values (in meV) deduced in photoemission experiments for $2H$-$NbSe_2$ in the Se pocket around Γ as well as in the Nb cylinders around Γ and $K$.

| Work | Gap (in meV) for each Fermi branch | | |
|---|---|---|---|
| | Se pocket | Nb (Γ) | Nb ($K$) |
| Kiss et al. [48] | - | 0.65±0.05 | - |
| Yokoya et al. [47] | 0 | 1 ± 0.1 | 0.9 ±0.1 |
| Kiss el al. [50] | 0 | 0.9-1.1 | 0.3-1.1 |
| Borisenko et al. [51] | - | 0-0.5 | 0.8 |
| Rahn et al. [52] | 0 ±0.2 | 0.1 ±0.3 | 2.3-2.6 ±0.2 |

## V. DISCUSSION

### A. Linking the small and large gaps to the Fermi surface sheets

The study of the band structure of $2H$-$NbSe_2$ by means of DFT calculations gives the respective contributions of the different Fermi surface sheets to the DOS at the Fermi level (see Table I). Moreover, from the tunneling data, we have deduced the empirical ratio of the partial DOS corresponding to the small and the large gaps: $N_S(E_F)/N_L(E_F) \sim 1/3$. This information allows the identification in $k$-space of the Fermi sheets corresponding to the small and large gaps, or at least to propose a reasonable scenario.

For simplicity in the discussion, we call the cylinders centered on the Γ point (respectively the $K$ point) of the Brillouin zone the ‘Nb Γ-cylinders’ (respectively the ‘Nb $K$-cylinders’) since they mostly arise from the Nb bands. The role of the additional Se Γ-pocket, see Fig.

14, will be discussed subsequently. We first assume that the two 'Nb Γ-cylinders' (or alternatively the two 'Nb $K$-cylinders') quasi overlap. If one adds the DOS contribution of band 2 and 3 around Γ ('Nb Γ-cylinders'), one obtains 0.7 elect.eV$^{-1}$.unit cell$^{-1}$ (i.e. 26 percent of the total DOS) while the contribution of bands 2 and 3 around $K$ gives 1.9 elect.eV$^{-1}$.unit cell$^{-1}$ (i.e. 70 percent of the total DOS). Thus, the ratio between the two partial DOS ($K$ as compared to Γ) is 0.37, a value which is very close to that inferred from the tunneling data. The immediate conclusion is that the small gap is associated with the 'Nb Γ-cylinders' and the large gap with the Nb $K$-cylinders.

However, as shown in Fig. 13 (blue line), the contribution of the 'Nb Γ-cylinders' to tunneling should dominate over that of the 'Nb $K$-cylinders'. On the other hand, as already described, the tunneling current is mostly sensitive to states with small $k_{\|}$ since the wave function decreases exponentially into the vacuum as a function of the distance $z$ from the surface. Since the region of the first Brillouin zone (FBZ) with small $k_{\|}$ should dominate the tunneling current, this predicts that the'Nb Γ-cylinders' having the *small gap* should reveal in the tunneling DOS. This is not observed in the experimental spectra [5, 9, 29].

To resolve this apparent paradox, there are two important aspects that must be taken into account: First, the existence of the Se pancake pocket around Γ and second, the charge density wave state coexisting at low temperature. Both of them have strong implications for the tunneling selectivity and the interband coupling, as we discuss below. The existence of the Se-based pancake (Figs. 9 and 14) has been confirmed experimentally, for instance using ARPES [10, 18] or magnetoresistance, [17] and is based on the Se $p_z$ orbitals. Thus it should strongly contribute to the tunneling current and is likely coupled to the Nb bands. Nevertheless, its role in multigap superconductivity is far from being understood.

The second aspect to consider is that the low temperature Fermi surface may be more complex than indicated in Fig. 14 due to the CDW state existing below the transition temperature $T_{CDW} \approx 35$K [3]. In the CDW state the system exhibits a nearly commensurate ($3a\times3a\times c$) superstructure [3, 21, 26]. This may play a significant role in both the interband coupling as well as in the tunneling selectivity. In fact, the consideration of the CDW state leads to a qualitative model in good agreement with the tunneling measurements.

Assuming a commensurate ($3a\times3a\times c$) superstructure after the transition, the CDW leads to a reduced hexagonal Brillouin zone with 1/9th of the parent area and centered at Γ. However, it is instructive to consider the extended zone scheme and to look for equivalent $k$ points in the non-reduced (parent) Brillouin zone. In particular, as a result of the new periodicity, the center of the FBZ, Γ, becomes equivalent to the parent $K$ point since $\Gamma\vec{K} = \vec{g_1} + \vec{g_2}$, with $\vec{g_2} = \frac{1}{3}\vec{G_2}$ and $\vec{g_3} = \frac{1}{3}\vec{G_3}$ (where $\vec{G_i}$ are the basis vectors of the parent reciprocal lattice of

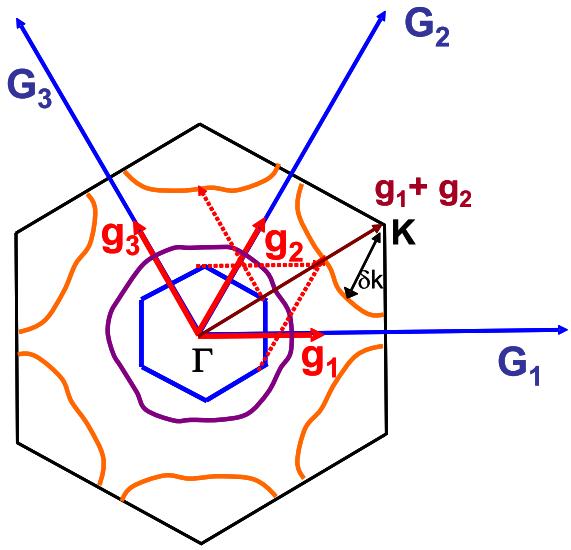


FIG. 14: (Color online) Schematic view of the Fermi surface of $2H$-$NbSe_2$. The vectors of the charge density wave $\vec{g_i} = \frac{1}{3}\vec{G_i}$ (where $G_i$ are the basis vectors of the reciprocal space of $2H$-$NbSe_2$ above the CDW phase transition temperature) link the selenium pocket around Γ (dark blue lines) to the cylinders around K (orange lines) at different points.

$2H$-$NbSe_2$). Consequently, in the tunneling probability, one has to consider $\alpha_k = \sqrt{\delta k^2 + \kappa^2}$ where $\delta\vec{k}$ is a vector from the $K$ point to the nearest FS sheet. Clearly, due to the CDW state, the $K$-cylinders are now considerably more favorable for the tunneling conductance.

The CDW state might also play a role in the interband coupling. As seen in Fig. 14, two wave vectors of the charge density wave $\vec{g_2} = \frac{1}{3}\vec{G_2}$ and $\vec{g_3} = \frac{1}{3}\vec{G_3}$ precisely link the small selenium pocket around Γ to the cylinders around $K$ at different points. For this reason, we expect a strong coupling mediated by the charge density wave between those two bands (or Fermi sheets). As will be shown in the following section, when the coupling is sufficiently strong ($\geq 10$ meV), the Se Γ-pocket and the Nb $K$-cylinders behave as one single band.

### B. Three band model calculation

The strong coupling effect may be further illustrated by a three-band model calculation. Let us consider three bands (see Fig. 15) with intrinsic gaps $\Delta_1^0 = 0$ meV, $\Delta_3^0 = 0$ meV, and $\Delta_2^0 = 1.4$ meV. The parameters of bands 1 and 2 correspond to the values found for the small gap (band 1) and large gap (band 2) of $2H$-$NbSe_2$. Band 1 is thus weakly coupled to band 2 and very weakly coupled to band 3. We then studied the evolution of the partial DOS in each band as a function of the interband coupling parameter $\Gamma_{32}$ between bands 2 and 3. The ratios of the interband scattering parameters have been chosen such that they correspond to the calculated DFT

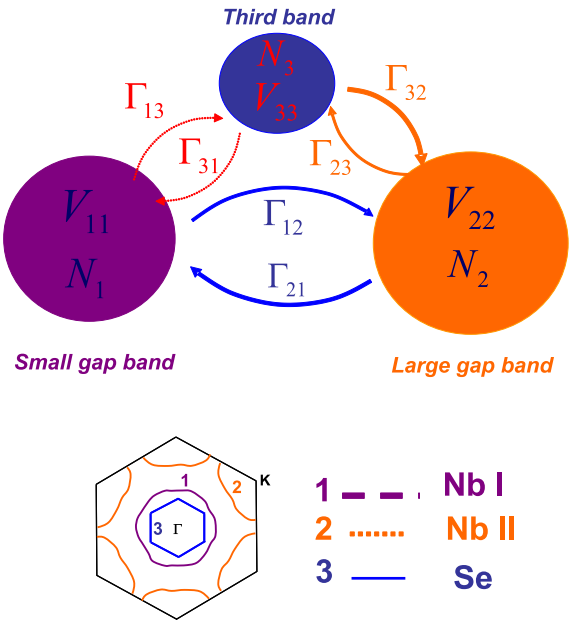


FIG. 15: (Color online) Schematic view of the possible interband couplings between those bands associated with the three different Fermi surface components. Band 1 (2) corresponds to the Nb cylinders around Γ ($K$), while band 3 corresponds to the Se pocket around Γ.

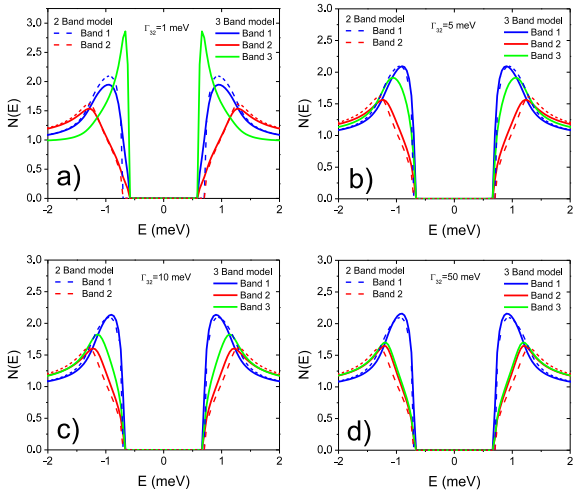


FIG. 16: (Color online) Partial DOS calculated for a three band model for different values of the interband coupling parameter between band 2 and band 3: a) $\Gamma_{32} = 1$ meV; b) $\Gamma_{32} = 5$ meV; c) $\Gamma_{32} = 10$ meV; d) $\Gamma_{32} = 50$ meV. The intrinsic gaps are $\Delta_1^0 = 0.$ meV, $\Delta_2^0 = 1.4$ meV, and $\Delta_3^0 = 0.$ meV. The ratio of the partial DOS at the Fermi energy are related to the ratio of quasiparticle scattering between the corresponding bands $\frac{N_1(E_F)}{N_2(E_F)} = \frac{\Gamma_{21}}{\Gamma_{12}} = 1/3$; $\frac{N_3(E_F)}{N_2(E_F)} = \frac{\Gamma_{23}}{\Gamma_{32}} = 1/16$; $\frac{N_3(E_F)}{N_1(E_F)} = \frac{\Gamma_{13}}{\Gamma_{31}} = 1/6$; The quasiparticle scattering parameters are: $\Gamma_{12} = 3$ meV; $\Gamma_{21} = 1$ meV; $\Gamma_{31} = 1$ meV.

ratios of the partial DOS (we recall that band 1 is associated with the 'Nb Γ-cylinders', band 2 with the Nb $K$-cylinders and band 3 with the Se pocket around Γ).

The interband coupling between bands 2 and 3 leads to an induced gap in band 3. As seen in Fig. 16, when $\Gamma_{32}$ increases, the DOS in band 3 is getting close to that in band 2. For very large $\Gamma_{32} \geq 50$ meV, one recovers a situation very similar to an effective two-band model with a new effective band constituted by bands 2 and 3. Thus, for a large coupling strength the model shows that bands 2 and 3 are indistinguishable from one single band. In Fig. 17 we plot the corresponding tunneling conductance assuming a complete tunneling selectivity towards band 3 (i.e. with tunneling weights $T_1 = 0$; $T_2 = 0$; $T_3 = 1$). For a large coupling $\Gamma_{32} \geq 50$ meV, the tunneling conductance is very close to that predicted in the two-band model, with a complete selectivity towards the band with the large gap.

In summary, we propose that the CDW state has strong implications for both the interband coupling as well as the tunneling measurement. The associated reduced reciprocal vectors imply the possible coupling between Nb derived FS sheets, but also give rise to the strong contribution to the tunneling conductance of the states around $K$, an essential ingredient for the observation of the large gap in $c$-axis tunneling spectra. However, in this model there should also be an important contribution to the tunneling current of the Se Γ-pocket. The necessary implication is that the Se pocket must be strongly coupled to the 'Nb $K$-cylinders' thus leading to an effective single band with a large gap.

Two experimental observations seem to confirm our model: First, the sensitivity of the tunneling selectivity upon cleavage. In fact, one expects significant variations of this small pocket with the surface conditions and most probably of the CDW state, which could then affect the coupling between the Se pocket and the Nb $K$-cylinders. Second, the tunneling spectra in the related material $NbS_2$, where no CDW has been observed [54], are very similar to those for $2H$-$NbSe_2$ but with a different tunneling selectivity, as explained in section V C.

### C. Comparaison with $NbS_2$

It is also interesting to compare the spectrum obtained for $2H$-$NbSe_2$ to that reported by Guillamón et al. for $2H$-$NbS_2$ [53]. This material is close to $2H$-$NbSe_2$, with a superconducting transition temperature of $T_C$= 5.7 K but does not exhibit any charge density wave instability [54]. Fitting their data with a two-gap model we obtain parameters close to those for $2H$-$NbSe_2$. The intrinsic gaps are: $\Delta_S^0 = 0 \pm 0.05$meV and $\Delta_L^0 = 1.15 \pm 0.05$meV. $\Gamma_{SL}$=1.5 meV and a ratio $\frac{\Gamma_{LS}}{\Gamma_{SL}} = 1/3 \pm 0.3$. The selectivity weights corresponding to the tunneling towards the two different effective bands are: $T_S = 0.4$ and $T_L = 0.6$.

We thus find that, as for $2H$-$NbSe_2$, superconductivity develops in one band (or more precisely in one Fermi surface sheet) whereas it is induced in the other by means

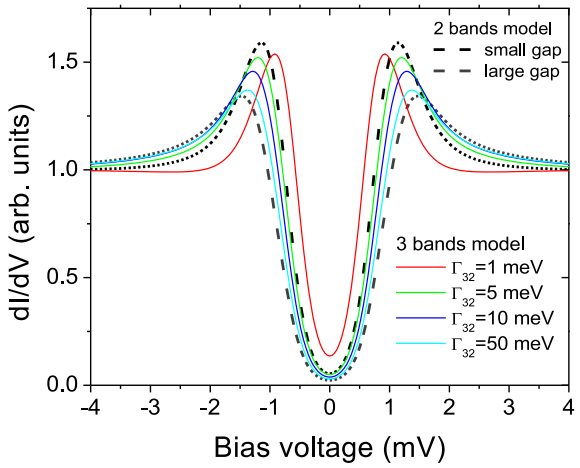


FIG. 17: (Color online) Tunneling conductance $dI/dV$ calculated in the three band model for different values of the interband coupling parameter between bands 2 and 3: $\Gamma_{32} = 1$, 5, 10, 50 meV; Dashed line: Tunneling conductance expected for the small and large gap in the two band model.

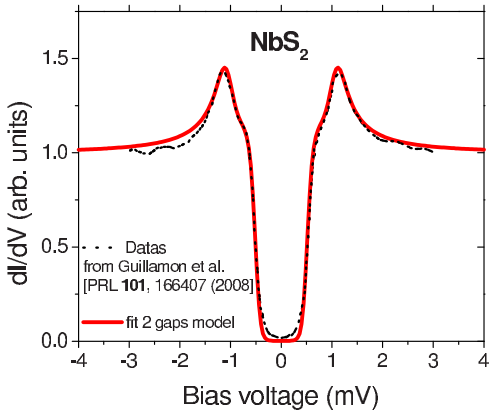


FIG. 18: (Color online) Tunneling conductance $dI/dV$ from Guillamón et al. [53] and fit obtained with the two gap McMillan equations. The parameters for the fit are the following. The intrinsic gaps are: $\Delta_S^0 = 0 \pm 0.05$meV and $\Delta_L^0 = 1.15 \pm 0.05$meV. $\Gamma_{SL}$=1.5 meV and $\frac{\Gamma_{LS}}{\Gamma_{SL}} = 1/3 \pm 0.3$. The selectivity weights corresponding to the tunneling towards the two different effective bands are $T_S = 0.4$ and $T_L = 0.6$. Note the we use a temperature for the fit The intrinsic gaps are: $\Delta_S^0 = 0 \pm 0.05$meV and $\Delta_L^0 = 1.15 \pm 0.05$ meV. $\Gamma_{SL}$=1.5 meV and a ratio $\frac{\Gamma_{LS}}{\Gamma_{SL}} = 1/3 \pm 0.3$. The selectivity weights corresponding to the tunnelling towards the two different effective bands are $T_S = 0.4$ and $T_L = 0.6$. Note that we use a temperature for the fit ($T_{fit} = 0.5$K) which is significantly higher than the experimental temperature ($T_{exp} = 0.1$K).

of interband coupling mediated by quasiparticle scattering from one band to the other. On the other hand, it is clear from the fits that the tunneling selectivity differs from $2H$-$NbSe_2$. As a matter of fact, there is an important contribution of the band with the small gap to the tunneling current.

In principle, this result could be explained in two different ways. First, although there is no CDW transition in $2H$-$NbS_2$, [54] our calculations show that the Fermi surface is very similar to that of $2H$-$NbSe_2$. In particular the pancake around $\Gamma$ is also present. This is a quite robust result since calculations for reasonable changes in the cell constants lead to small changes in the FS shape. The implication of these results is that the S based pancake pocket can *not* follow the previous mechanism based on a strong coupling with the '$K$-cylinders'. Consequently, it must couple only weakly to the cylinders around $\Gamma$ or $K$, and thus develop a small gap. Second, it could be argued that the S pocket has no states at the Fermi level at the surface layer. In this case, the $c$-axis tunneling originates primarily from both the Nb cylinders around $\Gamma$ and $K$, as shown in section III E. The simplest origin one could think for the suppression of the S based pancake,would be the occurrence of S vacancies which will raise the Fermi level. Using the bulk calculations we estimate that a large number of vacancies (i.e. $\sim$ 15%) are needed. Thus, this mechanism does not seem quite likely. We conclude that the absence of CDW strongly alters the coupling of the pancake with the cylinders and is eventually responsible for the differences between $2H$-$NbS_2$ and $2H$-$NbSe_2$.

## VI. CONCLUSION

We have measured the tunneling spectra of $2H$-$NbSe_2$ for two different orientations. The tunneling conductance can be properly described by a two band model, with gap values $\Delta_L^0 = 1.4$ meV and $\Delta_S^0 = 0.$ meV, where the interband coupling is provided by the scattering of quasiparticles from one band to the other. The data show evidence of a strong tunneling selectivity which depends on the orientation: the large gap is mainly probed along the '$c$' axis while this is the opposite along the $a/b$ axis.

In order to understand these results, we have calculated the DFT band structure of $2H$-$NbSe_2$. The Fermi surface contains three different components: a pancake like Se based contribution around $\Gamma$, and two pairs of Nb based cylinders parallel to $c^*$ around $\Gamma$ and $K$, respectively. The calculated values for the partial DOS associated with the three different components at the Fermi energy suggest that the large gap is associated with the cylinders around K. The calculation also suggests that when the CDW periodicity is not taken into account, the tunneling current is dominated by the $p_z$ character of the Se orbitals and depends on the way they couple to the 'Nb cylinders'.

On the basis of these electronic structure calculations, we have shown that the tunneling selectivity and the double-gap spectra are fully reconciled when the new pe-

riodicity imposed by the charge density wave is taken into account. Indeed, the latter has strong implications for the states probed in the tunneling measurement and provides the physical basis for a strong coupling of the Se pocket to the Nb '$K$-cylinders'.

## Appendix A

### 1. Computational details

The present calculations were carried out using a numerical atomic orbitals density functional theory (DFT) approach [55, 56], which was developed for efficient calculations in large systems and implemented in the SIESTA code [57, 58]. We have used the generalized gradient approximation (GGA) to DFT and, in particular, the functional of Perdew, Burke and Ernzerhof [59]. Only the valence electrons are considered in the calculation, with the core being replaced by norm-conserving scalar relativistic pseudopotentials [60] factorized in the Kleinman-Bylander form [61]. The non-linear core-valence exchange-correlation scheme [62] was used for all elements. We have used a split-valence double-$\zeta$ basis set including polarization functions, optimized for the bulk structure of $NbSe_2$ [63]. The energy cutoff of the real space integration mesh was 300 Ry. The Brillouin zone was sampled using a grid of (30×30×30) $k$-points within the Monkhorst-Pack scheme [64]. The experimental crystal structure was used for the bulk calculations. A symmetrical slab ten and a half unit cells thick based on the experimental bulk structure was used for the calculation of the STM images. In that case we also used an extra diffuse orbital in the basis set so as to take into account the slab nature of the system [65] and the Brillouin zone was sampled using a mesh of (30×30×1) $k$-points. The geometry of the ($3a$×$3a$×$c$) superstructure was optimized.

### 2. Qualitative understanding of the density of states

The features of the density of states at the Fermi level can be understood on the basis of the analysis of the wave functions. The two partially filled niobium-based bands, though more heavily based on the metal atoms, contain substantial niobium-selenium antibonding character. The dispersion of these bands results from a subtle equilibrium between direct in plane niobium-niobium interactions (ultimately responsible for the 30 K structural distortion) [22] and niobium-selenium antibonding interactions.

Increasing the niobium $d_{z^2}$ participation in the wave function is accompanied by an increase of the participation of the selenium $p_z$ orbitals. Roughly speaking, increasing the weight of $d_{z^2}$ in the wave function makes the Fermi surface more isotropic in the layer plane and shifts electron density from antibonding levels to the interlayer direction so that the mixing of niobium $d_{z^2}$ orbitals will be less favorable for the subband associated with the interlayer antibonding interactions. Increasing the niobium $d_{z^2}$ participation (and thus the selenium $p_z$ orbitals) increases the interlayer dispersion and reduces the density of states. Thus, keeping in mind the results of Fig. 8, it is easy to understand that the density of states at the Fermi level for both bands is larger for the cylinder around $K$ and that the effect is larger for the upper, interlayer antibonding band. It is also clear that the cylinders around Γ should be more isotropic than those around $K$.

### 3. Effect of the CDW on the band structure

Since our analysis is based on the room temperature crystal structure whereas the tunneling images are obtained at temperatures below the 30 K transition we must consider if the structural distortion may noticeably affect the results. The experimental structure of the low temperature phase has not been previously reported so that we carried out a structural optimization using a ($3a$×$3a$×$c$) supercell with fixed cell parameters. We obtained a structure exhibiting a niobium clustering pattern closely related to that proposed by Brouwer and Jellinek [26].

The projected densities of states for niobium $d_{z^2}$, niobium $d_{xy}/d_{x^2-y^2}$ and selenium corresponding to the distorted (noted 3×3) and undistorted (noted 1× 1) structures are compared in Figure 19. It is clear that the differences around the Fermi level are very small so that the main conclusions of the previous analysis should still hold after the 30 K transition. This is in keeping with early resistivity and heat-capacity measurements [66, 67] suggesting that the decrease in the density of states at the Fermi level should be of the order of only 1%. It is also in agreement with an independent theoretical study by Calandra *et al* [39]. Note the absence of any sign of gap opening at the Fermi level, something which is in agreement with recent atomic-scale scanning tunneling microscopy results, [68] which excludes a Fermi surface nesting mechanism for the 30 K transition. [18, 22, 23]

### 4. Discussion on the contribution of the Γ and $K$ cylinders to the tunneling current

For most values of the tip-to-surface distance, the contribution of the cylinders around Γ to the tunneling intensity is around twice larger than that of the cylinders around $K$ (Fig. 13). This may seem a bit surprising if we recall that the respective contributions to the density of states at the Fermi level were found to be just the opposite. However, this is in line with the results of the above mentioned fits (see Table II).

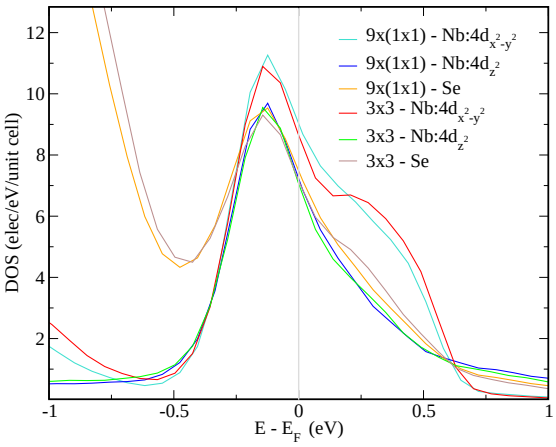


FIG. 19: (Color online) Comparison of the niobium $d_{z^2}$, niobium $d_{xy}/d_{x^2-y^2}$ and selenium contributions for the normal and CDW states.

One can think about two possible origins for this reversal. First, the faster decaying of the contribution of the cylinders around $K$ is due to the **k**-selectivity of the tunneling current [42]. It follows from Eq. 6 that the contribution to the tunneling of Fermi surface states with wave vectors near the Brillouin zone center ($\mathbf{k} = 0$) should be larger. Consequently, the contribution of the cylinders around Γ should become larger because of this effect and maybe could overcome the initial difference in density of states at the Fermi level. However, in the present case we evaluate the effect of this **k**-selectivity as leading at most to an increase of about 10 % of the calculated value. Consequently, this should not be the main factor behind the dominance of the contribution of the cylinders around Γ. Second, one should be aware that the decay of the Se $p_z$ orbitals is slower than the decay of the Se ($p_x$,$p_y$) orbitals. As discussed in detail in section III A, the nature of the niobium orbitals for the Fermi surface states associated with the cylinders around Γ and those around $K$ is different and this will induce a different hybridization of the selenium orbitals in the respective wave functions. As shown in Table I the relative weight of the Se $p_z$ vs. Se ($p_x$,$p_y$) orbitals is larger for the cylinders around Γ. This means that the hybridization between the Se orbitals is more strongly dominated by the $p_z$ orbitals for the states associated with the cylinders around Γ thus leading to a slower decay of these states.

A complementary aspect one must consider is that the plots of the density of states lack an important ingredient in order to understand a directional effect like the tunneling current along a certain direction: the signs of the mixing coefficients of the orbitals for a given wave vector. Of course these signs are directly related to the directionality of the electronic states and consequently strongly influence the tunneling in a given direction. Briefly speaking, the different nature of the niobium orbitals for the states around Γ and around $K$ lead to different Se orbitals hybridizations with a stronger control of the $p_z$ orbitals for the cylinder states around Γ. Actual calculation of the wave functions for points of the Fermi surface associated with the cylinders around Γ and around $K$ show that the former exhibit a slower decaying along $c$.


[1] E. Revolinsky, E. P. Lautenschlager, and C. H. Armitage, Solid State Comm., **1**, 59 (1963).
[2] E. Revolinsky, G. A. Spiering, and D. J. Beernsten, J. Phys. Chem. Solids **26**, 1029 (1965).
[3] J. A. Wilson, F. J. Di Salvo, and S. Mahajan, Phys. Rev. Lett. **32**, 882 (1974).
[4] R. C. Morris and R. V. Coleman, Phys. Lett. A **43** , 11 (1972).
[5] H. F. Hess, R. B. Robinson, and J. V. Waszczak, Phys. Rev. Lett. **64**, 2711 (1990).
[6] L. F. Mattheiss, Phys. Rev. Lett. **30**, 784 (1973).
[7] N. F. Doran, B. Ricco, M. Schreiber, D. Titterington, and G. Wexler, J. Phys. C **11** , 699 (1978)
[8] N. J. Doran, J. Phys. C **11**, 959 (1978).
[9] J. G. Rodrigo and S. Vieira, Physica C **404**, 306 (2004).
[10] T. Yokoya, T. Kiss, A. Chainani, S. Shin, M. Nohara, and H. Takagi, Science **294**, 2518 (2001).
[11] E. Boaknin, M. A. Tanatar, J. Paglione, D. Hawthorn, F. Ronning, R. W. Hill, M. Sutherland, L. Taillefer, J. Sonier, S. M. Hayden, and J. W. Brill, Phys. Rev. Lett. **90**,117003 (2003); E. Boaknin, M. A. Tanatar, J. Paglione, D. G. Hawthorn, R. W. Hill, F. Ronning, M. Sutherland, L. Taillefer, J. Sonier, S.M. Hayden, and J.W. Brill, Physica C **408-410**, 727 (2004).
[12] C. L. Huang, J.-Y. Lin, Y, T, Chang, C. P. Sun, H. Y. Shen, C. C. Chou, H. Berger, T. K. Lee, and H. D. Yang, Phys. Rev. B **76**, 212504 (2007).
[13] Yan Jing, Shan Lei, Wang Yue, Xiao Zhi-Li, and Wen Hai-Hu, Chin. Phys. B **17**, 2229 (2008).
[14] J. D. Fletcher, A. Carrington, P. Diener, P. Rodière, J. P. Brison, R. Prozorov, T. Olheiser, and R. W. Giannetta, Phys. Rev. Lett. **98**, 057003 (2007).
[15] H. Suhl, B. T. Matthias, and L. R. Walker, Phys. Rev. Lett. **3**, 552 (1959).
[16] J. Bardeen, L. Cooper, and J. Schrieffer, Phys. Rev. **108**, 1175 (1957).
[17] R. Corcoran, P. Meeson, Y. Onuki, P.-A. Probst, M. Springford, K. Takita, H. Harima, G. Y. Guo, and B. L. Gyorffy, J. Phys.: Condens. Matter **6**, 4479 (1994).
[18] K. Rossnagel, O. Seifarth, L. Kipp, and M. Skibowski, D. Voß, P. Krüger, A. Mazur, and J. Pollmann, Phys. Rev B. **64**, 235119 (2001).
[19] A. Meerschaut and C. Deudon, Mat. Res. Bull. **36**, 1721 (2001).
[20] M. Marezio, P. D. Dernier, A. Menth, and G. W. Hull Jr., J. Solid State Chem. 4, 425 (1972).
[21] J. A. Wilson, F. J. DiSalvo, and S. Mahajan, Adv. Phys. **24**, 117 (1976).
[22] M.-H. Whangbo and E. Canadell, J. Am. Chem. Soc. **114**, 9587 (1992).

[23] M. D. Johannes, I. I. Mazin, and C. A. Howels, Phys. Rev. B **73**,205102 (2006).

[24] T. M. Rice and G. K. Scott, Phys. Rev. Lett. **35**, 120 (1975).

[25] D. E. Moncton, J. D. Axe, and F. J. DiSalvo, Phys. Rev. B **16**, 801 (1977).

[26] R. Brouwer and F. Jellinek, Physica B **99**, 51 (1980).

[27] H. Schmidt, J. F. Zasadzinski, K. E. Gray, and D. G. Hinks, Physica C **385**, 221 (2003).

[28] W. L. McMillan, Phys. Rev. **175**, 537 (1968).

[29] Y. Noat, T. Cren, F. Debontridder, D. Roditchev W. Sacks, P. Toulemonde, and A. San Miguel, Phys. Rev. B **82**, 014531 (2010).

[30] J. Kortus, O. V. Dolgov, and R. K. Kremer, Phys. Rev. Lett. **94**, 027002 (2005).

[31] P. Szabó, P. Samuely, J. Kačmarčík, T. Klein, J. Marcus, D. Fruchart, S. Miraglia, C. Marcenat, and A. G. M. Jansen, Phys. Rev. Lett. **87**, 137005 (2001).

[32] F. Giubileo, D. Roditchev, W. Sacks, R. Lamy, D. X. Thanh, J. Klein, S. Miraglia, D. Fruchart, J. Marcus, and P. Monod, Phys. Rev. Lett. **87**, 177008 (2001).

[33] G. Karapetrov, M. Iavarone, A. E. Koshelev, W. K. Kwok, G. W. Crabtree, and D. G. Hinks, S. I. Lee, Physica C **388** –**389**, 141 (2003).

[34] M. Iavarone, G. Karapetrov, W. K.Kwok, G. W. Crabtree, D. G. Hinks, W. N. Kang, E.-M. Choi, H. J. Kim, H.-J. Kim, and S. I. Lee, Phys. Rev. Lett. **89**, 187002 (2002).

[35] H. Schmidt, J. F. Zasadzinski, K. E. Gray, and D. G. Hinks, Phys. Rev. Lett. **88**, 127002 (2002).

[36] N. Schopohl and K. Scharnberg, Solid State Commun. **22**, 371 (1977).

[37] H. J. Choi, D. Roundy, H. Sun, M. L. Cohen, and S. G. Louie, Nature **418**, 758 (2002).

[38] The parameters used for the fit are slightly different from those deduced at $T = 2K$. This might come from different cleavage conditions. One also notes that the fit deviates from the data inside the gap for bias voltages close to the excitation gap. This can be explained in terms of a three band model, which takes into account the effect of the Se pocket, as explained in section V B.

[39] M. Calandra, I. I. Mazin, and F. Mauri, Phys. Rev. B **80**, 241108(R) (2009).

[40] G. Wexler and A. M. Wolley, J. Phys. C **9**, 1185 (1976).

[41] T. Straub, T. Finteis, R. Claessen, P. Steiner, S. Hufner, P. Blaha, C. S. Oglesby, and E. Boucher, Phys. Rev. Lett. **82**, 4504 (1999).

[42] J. Tersoff and D. R. Hamman, Phys. Rev. B **31**, 805 (1985).

[43] P. Mallet, W. Sacks, D. Roditchev, D. Défourneau, and J. Klein, J. Vac. Sci. Technol. B **14**, 1070 (1996).

[44] M. Nohara, M. Isshiki, F. Sakai and H. Takagi, J. Phys. Soc. Jpn. **68**, 1078 (1999).

[45] T. Hanaguri, A. Koizumi, K. Takaki, M. Nohara, H. Takagi, K. Kitazawa, Physica B **329-333**, 1355 (2003).

[46] D. Sanchez, A. Junod, J. Muller, H. Berger, F. Lévy b, Physica B **204**, 167 (1995).

[47] T. Yokoya, T. Kiss, A. Chainani, S. Shin,M. Nohara, H. Takagi, Science, **294**, 2518 (2001)

[48] T. Kiss,T. Yokoya, A. Chainani, S. Shin, M. Nohara, H. Takagi, Physica B **312313**, 666 (2002).

[49] T. Valla, A.V. Fedorov, P. D. Johnson, P-A. Glans, C. McGuinness, K. E. Smith, E.Y. Andrei, H. Berger, Phys. Rev. Lett. **92**, 086401 (2004).

[50] T. Kiss, T. Yokoya, A. Chainani, S. Shin, T. Hanaguri, M. Nohara and H. Takagi, Nature Physics **3**, 720 (2007).

[51] S.V. Borisenko, A. A. Kordyuk, V. B. Zabolotnyy, D. S. Inosov, D. Evtushinsky, B. Büchner,1 A. N. Yaresko,A. Varykhalov, R. Follath, W. Eberhardt, L. Patthey and H. Berger, Phys. Rev. Lett. **102**, 166402 (2009).

[52] D. J. Rahn, S. Hellmann, M. Kalläne, C. Sohrt, T. K. Kim, L. Kipp, K. Rossnagel, Phys. Rev. B **85**, 224532 (2012).

[53] I. Guillamón, H. Suderow, S. Vieira, L. Cario, P. Diener, and P. Rodière, Phys. Rev. Lett. **101**, 166407 (2008).

[54] Y. Hamaue and R. Aoki, J. Phys. Soc. Jpn. **55**, 1327 (1986).

[55] W. Kohn and P. Hohenberg, Phys. Rev. B **136**, 864 (1964).

[56] W. Kohn and L. J. Sham, Phys. Rev. A, **140**, 1133 (1965).

[57] J. M. Soler, E. Artacho, J. Gale, A. García, J. Junquera, P. Ordejón, and D. Sánchez-Portal, J. Phys.: Condens. Matter **14**, 2745 (2002).

[58] E. Artacho, E. Anglada, O. Diéguez, J. D. Gale, A. García, J. Junquera, R. M. Martin, P. Ordejón, J. M. Pruneda, D. Sánchez-Portal, and J. M. Soler, J. Phys.: Condens. Matter **20**, 064208 (2008).

[59] J. P. Perdew, K. Burke, and M. Ernzerhof, Phys. Rev. Lett. **77**, 3865 (1996).

[60] N. Trouiller and J. L. Martins, Phys. Rev. B **43**, 1993 (1991).

[61] L. Kleinman and D. M. Bylander, Phys. Rev. Lett. **48**, 1425 (1982).

[62] S. G. Louie, S. Froyen, and M. L. Cohen, Phys. Rev. B **26**, 1738 (1982).

[63] E. Artacho, D. Sánchez-Portal, P. Ordejón, A. García, and J. M. Soler, Phys. Stat. Sol. (b) **215**, 809 (1999).

[64] H. J. Monkhorst and J. D. Pack, Phys. Rev. B **13**, 5188 (1976).

[65] S. García-Gil, A. García, N. Lorente, and P. Ordejón, Phys. Rev. B **79**, 075441 (2009).

[66] J. R. Long, S. P. Bowen, and N. E. Lewis, Solid State Commun. **22**, 363 (1977).

[67] J. M. E. Harper, T. H. Geballe, and F. J. DiSalvo, Phys. Lett. A **54**, 27 (1975).

[68] S. P. Chockalingam, C. J. Arguello, E. P. Rosenthal, L. Zhao, C. Gutiérrez, J. H. Kang, W. C. Chung, R. M. Fernandes, S. Jia, A. J. Millis, R. J. Cava, and A. N. Pasupathy, http://arxiv.org/pdf/1307.2282.